Article

Bioimaging and Biosensing of Ferrous Ion in Neurons and HepG2 Cells Upon Oxidative Stress

Zhichao Liu, Shengnan Wang, Wanying Li, and Yang Tian

Anal. Chem., **Just Accepted Manuscript** • DOI: 10.1021/acs.analchem.7b04934 • Publication Date (Web): 29 Jan 2018

Bioimaging and Biosensing of Ferrous Ion in Neurons and HepG2 Cells Upon Oxidative Stress

Zhichao Liu,[+] Shengnan Wang,[+] Wanying Li, and Yang Tian*

Shanghai Key Laboratory of Green Chemistry and Chemical Processes, Department of Chemistry, School of Chemistry and Molecular Engineering, East China Normal University, Dongchuan Road 500, Shanghai 200241, China

*E-mail: ytian@chem.ecnu.edu.cn

ABSTRACT: Iron ion as main component of intracellular labile iron, not only plays an important function in oxygen transport, enzymatic reactions, and electron transport, but is also vital important in oxidative stress. In this work, we developed a ratiometric fluorescent biosensor for ferrous ion (Fe^{2+}), in which gold nanoclusters (AuNCs) were synthesized as a stable fluorescent probe and a ligand (FeL) was designed for specific recognition of Fe^{2+} and conjugated onto AuNCs (AuNC@FeL). Meanwhile, water-soluble sulfo-cyanine 7 NHS ester (Cy7 NHS ester) was immobilized onto AuNC@FeL as a reference element. The developed ratiometric fluorescent nansosensor displayed a good linearity with the concentration of Fe^{2+} in the range of 1-105 μM and detection limit was achieved down to 210 nM. In addition, this nanosensor responded to Fe^{2+} less than 1.23 s and showed high selectivity against other metal ions, amino acids and reactive oxygen species. Taking the advantages of high selectivity and accuracy, as well as quick response and long-term stability, this organic-inorganic ratiometric fluorescent probe was successfully applied in real-time biosensing and bioimaging of Fe^{2+} in neurons and HepG2 cells. Using this useful tool, it was found that the increasing concentration of Fe^{2+} in live cells was closely related to oxidative stress.

INTRODUCTION

Iron as the most abundant transition metal in human body, participating in many physiological events such as oxygen transport,[1] enzymatic reactions,[2,3] and electron transport.[4] In living cells, labile iron mainly consists of Fe^{2+} ion owing to a reducing environment.[5] Fe^{2+} can promote oxidative stress via participating in process like Fenton reaction where hydroxyl radical and other reactive oxygen species (ROS) were generated, which is potentially harmful to cells.[6,7] Furthermore, iron metabolism and equilibrium between Fe^{2+}/Fe^{3+} have close link to large amount of diseases, like anemia,[8] kidney diseases,[9] hepatitis diseases,[10] and neurological disorders such as Alzheimer's and Parkinson's diseases.[11,12] Therefore, it is vital importance to develop analytical methods for Fe^{2+} detection in biological systems, which is helpful for understanding the functions and contributions of Fe^{2+} in living body.

Up to now, a lot of elegant analytical methods have been developed for determination of Fe^{2+}, including atomic absorption spectroscopy (AAS), inductively coupled plasma mass spectrometry (ICP-MS), electrochemical method, colorimetric and fluorescent spectroscopy, and so on.[13-20] Among these methods, fluorescent probe has been attracted much attention because of its high sensitivity and selectivity, non-invasive, and real-time sensing and imaging.[17-23] Our groups is very interested in development of analytical approaches for determination of metal ions and ROS. We have established several organic-inorganic ratiometric fluorescent nanosensors for detection of Cu^{2+}, Zn^{2+}, pH and other oxidative stress-related species in live cells and

tissues.[24-31] However, fluorescent probe for Fe^{2+} sensing is still a challenging work, because it is hard to design a dual-emission organic fluorophores for specific and sensitive determination of Fe^{2+} with good stability and rapid responsive dynamics. Actually, organic-inorganic ratiometric fluorescent nanoprobe may solve these problems, because organic ligand can provide selective recognition while inorganic nanomaterials such as carbon dots and gold nanoclusters demonstrate good fluorescence stability with low cytotoxicity.[32,33] Furthermore, the ratiometric determination is independence of probe concentration, the drift of light sources or detectors, and environmental effects in complex samples, resulting in high accuracy.[34,35]

In this work, fluorescent gold nanoclusters (AuNCs) were first synthesized using a template of glutathione (GSH), and a specific recognition ligand for Fe^{2+} ion (FeL) was designed and then conjugated onto AuNCs to produce fluorescent probe for Fe^{2+} (AuNC@FeL). Furthermore, water-soluble sulfo-cyanine 7 NHS ester (Cy7 NHS ester) was immobilized to AuNC@FeL as reference signal, resulting in ratiometric fluorescent nansosensor denoted as AuNC@FeL@Cy7 (Scheme 1). The developed organic-inorganic nanosensor shows two separated emissions around 622 nm and 820 nm when excited at 552 nm, which belong to those of AuNC@FeL and Cy7, respectively. The present ratiometric fluorescent nanosensor responded to Fe^{2+} less than 1.23 s and showed high selectivity for Fe^{2+} against Fe^{3+} and other metal ions, amino acids and ROS owing to the presence of specific FeL. In addition, the

fluorescence ratio of AuNC@FeL@Cy7 displayed a good linearity with the logarithmic concentration of Fe^{2+} in the range of 1-105 μM and detection limit for Fe^{2+} was achieved to 210 nM. Comparing with previous reported fluorescent Fe^{2+} probes,[18-20,36] the developed organic-inorganic ratiometric fluorescent probe demonstrated high accuracy with long-term fluorescence stability and rapid responsive dynamic, and successfully applied for biosensing and bioimaging of Fe^{2+} ion in neurons and HepG2 cells.

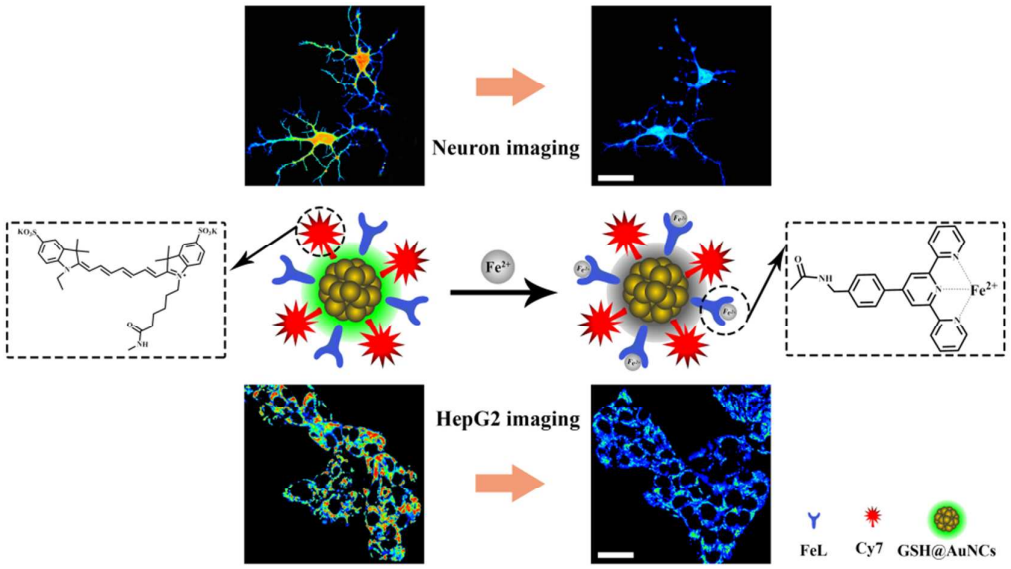

Scheme 1. Working principle of the developed AuNC@FeL@Cy7 ratiometric fluorescent probe for Fe^{2+} sensing and imaging. Scale = 25 μm.

EXPERIMENTAL SECTION

Reagents. 4-Cyanobenzaldehyde, lithium aluminium hydride (AlH_4Li), glutathione (GSH), 2-Acetylpyridine, sodium iodide (NaI), anhydrous sodium sulfate (Na_2SO_4), (4-carboxybutyl) triphenylphosphonium bromide (TPP) and 4-(2-aminoethyl) morpholine (AMP), 3-(4,5-dimethyl-2-thiazolyl)-2,5-diphenyl-2-H-tetrazolium

bromide (MTT), 1-(3-Dimethylaminopropyl)-3-ethylcarbodiimide hydrochloride (EDC), silicon (Si) powder, magnesium (Mg) powder, and chloroauric acid ($HAuCl_4$) were purchased from Aladdin Chemistry Co. Ltd. (China). Hydrazine hydrate ($N_2H_4 \cdot H_2O$), tetrahydrofuran (THF), dichloromethane (CH_2Cl_2), dimethyl sulfoxide (DMSO), methylbenzene, phosphorus oxychloride ($POCl_3$), sodium hydroxide (NaOH), PVP 30 (average relative molecular mass of 30,000) and sodium bicarbonate ($NaHCO_3$) were purchased from Sinopharm chemical reagent Co. Ltd. (China). Sulfo-Cyanine7 NHS ester was purchased from Lumiprobe Corporation (U.S.A.). poly-D-lysine (PDL), Neurobasal medium, B27, L-glutamin, minimum essential medium (MEM), trypsin, phosphate-buffered saline (PBS), Hoechst 33342, LysoTracker Green, MitoTracker Green and CellTracker Green CMFDA were purchased from Thermo Fisher scientific (U.S.A.). All chemicals were analytical grade and used without further purification. All samples were prepared by deionized water purified by Milli-Q water purification system.

Instruments. Nuclear magnetic resonance (NMR) spectra were recorded on a Bruker 500 MHz spectrometer (Bruker, Germany). Mass spectra (MS) were recorded by Agilent 6890 (Agilent, USA). The UV-Vis absorption spectra and fluorescence spectra were obtained with an UH5300 spectrophotometer (Hitachi, Japan) and F-4500 fluorescence spectrophotometer (Hitachi, Japan). X-ray photoelectron spectrum (XPS) was obtained by ESCALAB 250Xi (Thermo Fisher scientific, U. S. A.). Transmission electron microscope (TEM) images were collected with a JEM-2100F transmission

electron microscope (JEOL, Japan). Atomic force microscope (AFM) images were recorded in the ScanAsyst mode under ambient conditions (Bruker, Germany). Fourier transform infrared spectroscopy (FT-IR) spectra were obtained using a Thermo Scientific Fourier Transform Infrared spectrometer (Thermo Fisher scientific, U. S. A.) at resolution of 4 cm^{-1} in the range of 500-4000 cm^{-1}. The absorbance of cytotoxicity was recorded by a Varioskan LUX multimode microplate reader (Thermo Fisher scientific, U.S.A.). The apoptosis assay was conducted at a FACS Calibur flow cytometry (Becton, Dickinson and Company, U.S.A.). Fluorescence confocal imaging was performed with a Leica TCS-SP8 confocal scanning microscope using a 63× oil objective and a numerical aperture of 1.40 (Leica, Germany).

Synthesis of FeL. FeL was synthesized according to the literature with modification.[17] Briefly, 2-Acetylpyridine (15 mmol) was added into an anhydrous ethanol solution (50 mL) of 4-formylbenzonitrile (7.5 mmol). Then, NaOH (15 mmol) and $N_2H_4 \cdot H_2O$ (23 mL, 28.0%) was added to the solution, followed by stirring at 37ºC for 24 h. After the mixture cooled down to room temperature, the off-white solid was collected by filtration and washed with ice-cold anhydrous ethanol. White crystalline solid was recrystallized from anhydrous ethanol.

Next, anhydrous THF (35 mL) and AlH_4Li (13.2 mmol) were added into a 250 mL egg-shaped flask. The obtained product (2.99 mmol) was then dissolved in 35 mL of anhydrous THF and added into the egg-shaped flask drop-by-drop within 4 h by constant pressure funnel. The mixture was reacted overnight at 70ºC with a magnetic

stirrer under N_2 atmosphere. Hydrous THF was added into the mixture, and then the mixture was filtered. The filtered solution was vapored in a vacuum distillation system. The residue was dissolved in CH_2Cl_2 solution, and hydrogen chloride gas was pumped into above solution. After filtered the precipitation and dissolved it in aqueous solution, $NaHCO_3$ was added in order to neutralize the excess hydrochloric acid. An aqueous solution of the residue was extracted with CH_2Cl_2. Concentration of the extracts gave the desired product as a light yellow solid.

Preparation and purification of AuNCs. AuNCs were synthesized by chemical reduction of $HAuCl_4$ with GSH. Solution of GSH (15 mM) was added to an equal volume of 10 mM $HAuCl_4$. The mixture was vigorously stirred for 2 min, followed by the addition of 1 M NaOH (1 mL) to adjust pH to 12. Then, the solution was incubated at 37ºC under continuous stirring for 24 h. Excess GSH were removed by addition of excessive methanol into the aqueous solution (the ratio between water and methanol is 1:4) and then centrifuged at 15000 rpm for 5 min. The precipitates were separated and finally dispersed in water for further using.

Preparation of ratiometric fluorescent AuNC@FeL@Cy7 probe. FeL was first dissolved in DMSO to obtain a storage solution, then AuNCs solution and moderate FeL (molar ratio of AuNCs:FeL=1:1.2) were mixed at room temperature and EDC was added under stirring. The mixture was reacted at room temperature at least 6 h, and then purified by dialysis (molecular weight: 100-500 Da) to obtain AuNC@FeL. Next, sulfo-cyanine 7 NHS ester was added to the purified AuNC@FeL solution and

reacted at room temperature under stirring for at least 6 h. At last, the mixture was purified by ultrafiltration to obtain AuNC@FeL@Cy7 and stored at 4^{o}C away from light.

Preparation of organelle-targeted ratiometric fluorescent probe. For preparing the organelle-targeted probe, (4-carboxybutyl) triphenylphosphonium bromide (TPP) or 4-(2-aminoethyl) morpholine (AMP) was first dissolved in PBS buffer, then EDC and AuNC@FeL@Cy7 probe were added under stirring. Next, the mixture was reacted at room temperature for 6 h and then purified by dialysis (molecular weight: 100-500 Da) to obtain AuNC@FeL@Cy7@TPP and AuNC@FeL@Cy7@AMP probes.

Synthesis of Mg_2Si nanoparticles. Mg_2Si nanoparticles were synthesized according to literature.[37] Briefly, 100 mmol of Mg powder and 40 mmol of Si powder were mixed in a 25 ml alumina crucible. The mixture was heated at 500 °C for 3 h with a ramping rate of 10^{o}C min^{-1} under an Ar/O_2 (5% O_2) atmosphere. After cooled to room temperature, the resultant product was immersed in 200 ml of 95% ethanol solution containing 2 g of PVP 30, and then ultrasonicated at 60^{o}C for 5 h to hydrate MgO adequately. The subsequent suspension was gently centrifuged at 5000 rpm for 10 min to eliminate the insoluble $Mg(OH)_2$ and other large particles. The dispersed Mg_2Si nanoparticles were then collected by centrifugation at 13000 rpm for 15 min, and washed with ethanol three times.

Primary culture of mouse cortical neurons and HepG2 cells. The experimental protocols were approved by Animal Care and Use Committee of East China Normal

University, Shanghai, China. Primary cultures of mouse cortical neurons were prepared as described previously.[38] Briefly, postnatal day 1 C57BL/6 WT mice were anesthetized with halothane. Brains were removed rapidly and placed in ice-cold Ca^{2+}- and Mg^{2+}-free Hank's balanced salt solution (HBSS). Tissues were dissected and incubated with Papain for 15 min at 37°C, followed by trituration with fire-polished glass pipettes, and plated in PDL-coated 35-mm Petri dishes with 20 mm bottom wells at a density of 1×10^6 cells per dish. Neurons were cultured with Neurobasal medium supplemented with B27 and L-Glutamin, then maintained at 37°C in a humidified 5% CO_2 atmosphere incubator. Cultures were fed twice a week and used for all the assays 8-14 days after plating.

HepG2 cells were cultured in a 5% CO_2 incubator at 37°C with saturated humidity. HepG2 cells were cultured in MEM containing 10% fetal bovine serum and 1% penicillin/streptomycin solution.

Cytotoxicity and apoptosis assay. For cytotoxicity assay, different concentrations of AuNC@FeL@Cy7 probe were added into pre-incubated neurons and HepG2 cells in 96-well plates and cultured for 24 and 48 h, respectively. Subsequently, 20 μL MTT solutions were added to every well in dark. After reaction for 4 h, removing the mixed solution from every well and adding 80 μL DMSO into the well. Then shaking for 5 min and the absorbance was measured at 490 nm. Cell viability values were determined according to the following formulae: cell viability (%) = absorbance of the experimental group/ absorbance of the blank control group × 100%. For apoptosis

assay, different concentrations of AuNC@FeL@Cy7 probe were cultured with neurons or HepG2 cells for 24 h. After removing the culture media, the cells were collected with the help of EDTA-free trypsin. After washing with PBS, the cells were re-suspended in 300 μL binding buffer and incubated with 5 μL FITC-Annexin V and 5 μL propidium iodide solution for 30 min in the dark. The apoptosis assay was detected by Becton-Dickinson flow cytometer at an excitation wavelength of 480 nm.

Cell imaging. Neurons in dishes cultured with Neurobasal medium was replaced with HBSS containing the nanosensor (30 μM) and further incubated for 1 h. Thereafter, the adhered neurons were washed twice with HBSS to remove the nanosensors that were not taken up into the neurons. The multicolor Fe^{2+} imaging was conducted in HBSS containing different concentrations of Fe^{2+}.

For Fe^{2+} imaging in neurons under oxygen and glucose deprivation treatment, 30 μM nanosensor were first co-incubated with neurons for 1 h in different dishes, then adhered neurons were washed twice with PBS to remove the nanosensors that were not taken up into the neurons. Subsequently, the nanosensor-loaded neurons were cultured with PBS purged by nitrogen gas for 10 min, and then the neurons were placed in a chamber filled with 5% CO_2 and 95% N_2 atmosphere for different times before imaging. For recovery experiments, neurons were first cultured with PBS in an anaerobic chamber containing a 5% CO_2 and 95% N_2 atmosphere for 1 h, then PBS replaced as HBSS for culturing another 1 h in a humidified 5% CO_2 atmosphere. After that, 30 μM nanosensor were added and co-incubated for 1 h, then adhered neurons

were washed twice with HBSS to remove the nanosensors that were not taken up into the neurons before imaging.

For HepG2 cells imaging, HepG2 cells were first placed onto 35 mm plastic Petri dishes with 20 mm bottom well and cultivated for at least 12 h. Then, the medium was replaced by fresh PBS containing 30 μM nanosensor and further cultivated for 1 h. Thereafter, the adhered cells were washed twice with PBS to remove the nanosensors that were not taken up into the cells. The multicolor Fe^{2+} imaging was conducted in PBS containing different concentrations of Fe^{2+}. For Fe^{2+} imaging under hypoxia condition, 3 mM MSPs were added to nanosensor-loaded cells and co-incubated for 1 h before imaging.

RESULTS AND DISCUSSION

Synthesis and characterization of fluorescent nanosensor for Fe^{2+}. It is well-known that a nanosensor usually consists of two parts: one is recognition unit, another is response unit. In order to develop a fluorescent nanosensor for Fe^{2+}, we first synthesized an organic molecule for specific recognition of Fe^{2+}, 4'-(aminomethylphenyl)-2, 2':6', 2''-terpyridine, which was denoted as FeL (Scheme S1). The FeL molecule functionalized with $-NH_2$ group was characterized and confirmed by ^1H NMR, ^{13}C NMR, and MS (Figure S1-S4). On the other hand, GSH-based AuNCs were synthesized according to previous report with modification.[39] As shown in Figure 1A, TEM image shows the as-prepared AuNCs

were monodispersed with average size of 1.35±0.3 nm (Figure 1A insert). High resolution TEM image displays clear lattice plane with interplanar spacing of 0.23 nm, in accordance with the (111) crystal planes of face-centered-cubic Au.[40] Typical AFM image demonstrates that spherical AuNCs are separated well from each other with height of ~1.2 nm (Figure 1B). UV-vis absorption spectrum of AuNCs displays a board absorption band around 360 nm (Figure S5). The as-prepared AuNCs emits at ~685 nm when excited at 552 nm and shows jacinth fluorescence under excitation using a 365 nm UV lamp (Figure 1C and insert).

Next, the fluorescent probe for determination of Fe^{2+} was developed by conjugating FeL molecules onto AuNCs using EDC as a catalyst, which was denoted as AuNC@FeL. The emission of AuNCs blue-shifted to ~622 nm after FeL was coupled onto AuNCs to form AuNC@FeL (Figure 1C). This blue-shift by ~63 nm may be attributed to changes of AuNCs surface state after FeL conjugated onto AuNCs.[41] Furthermore, FT-IR spectroscopy was used to characterize the conjugated processes. As shown in Figure 1D, FeL molecule shows distinct peaks at 3356 and 1583 cm^{-1}, which are ascribed to the ν (N-H) and δ (N-H) bonds, respectively, indicating the presence of $-NH_2$ group on FeL. Meanwhile, obvious peaks observed at 3061, 1565 and 780 cm^{-1} are attribute to the ν (C-H), ν (C=C, C=N) and γ (C-H) of pyridine ring, further confirming the typical groups on FeL. In addition, FT-IR spectrum of AuNCs show three peaks located at 3301, 1653 and 1257 cm^{-1}, attributed to ν (-OH), ν (C=O) and ν (C-O), respectively. This means -COOH groups were

attached on the surface of AuNCs (Figure 1D). Interestingly, after FeL was conjugated onto AuNCs, obvious vibrations of ν (C=C, C=N) and γ (C-H) of pyridine ring were observed, proving the successful attachment of FeL onto AuNCs (Figure 1D).

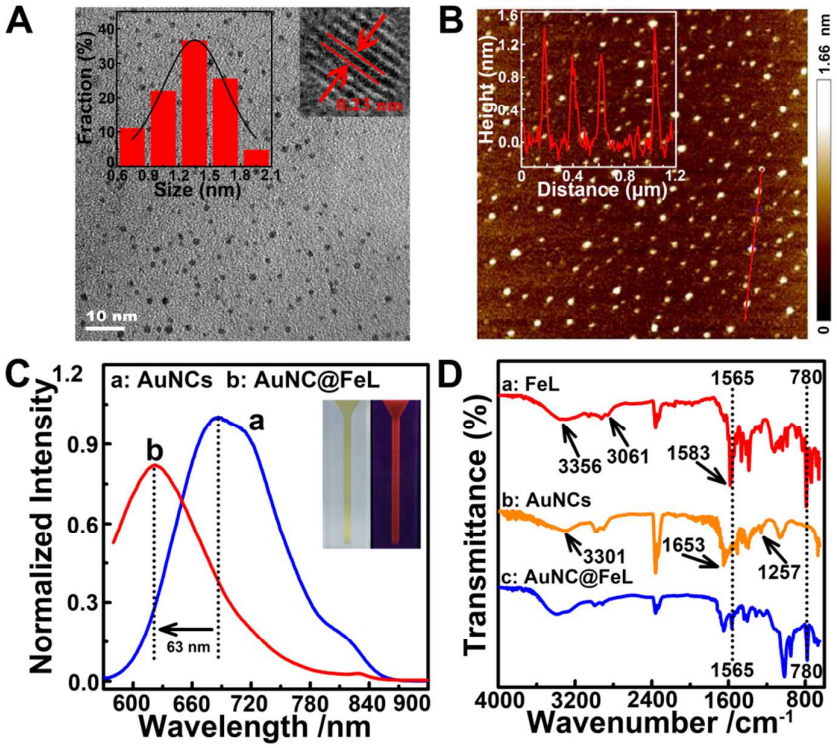

Figure 1. (A) Typical TEM image of AuNCs. The insets show the size distribution histogram (top left) and the high-resolution TEM image (top right) of AuNCs. (B) Typical AFM image of AuNCs. Inset shows height distribution of AuNCs along the line. (C) Fluorescence emission spectra of (a) AuNCs and (b) AuNC@FeL under excitation wavelength of 552 nm. Insert shows photographs of AuNCs solution under ambient light (left) and illuminated by an UV lamp of 365 nm (right). (D) FT-IR spectra of (a) FeL, (b) AuNCs, and (c) AuNC@FeL.

In vitro ratiometric determination of Fe^{2+}. Considering the advantages of ratiometric fluorescence nanosenor with high accuracy, we then developed a fluorescence probe for Fe^{2+} with inn-reference by immobilizing water-soluble

sulfo-cyanine 7 NHS ester (Cy7 NHS ester, Figure S6) onto AuNC@FeL to generate AuNC@FeL@Cy7 nanoprobe. FT-IR spectrum of fluorescent AuNC@FeL@Cy7 nanoprobe shows two obvious peaks at 1164 cm^{-1} and 1145 cm^{-1}, which are attributed to the asymmetric and symmetric stretching vibration of S=O bond from sulfo group. Meanwhile, the clear peak obtained at 785 cm^{-1} was due to stretching vibration of S-O from sulfo group, proving Cy7 was attached onto AuNCs@FeL surface (Figure S7). As demonstrated in Figure 2A, AuNC@FeL and Cy7 NHS exhibit well-separated fluorescent emission peaks around 622 nm and 820 nm, respectively, under one excitation at 552 nm. After Cy7 was immobilized onto AuNC@FeL, two emission peaks were observed at the range of 580-760 nm and 765-900 nm (Figure 2A). With the increasing concentration of Fe^{2+}, the fluorescence intensity of AuNCs (F_{green}: 580-760 nm) decreased dramatically while the fluorescence intensity of Cy7 (F_{red}: 765-900 nm) kept no obvious change (Figure 2B), confirming our prepared nanosensor can be used for Fe^{2+} detection with ratiometric fluorescence. The fluorescence intensity ratio (F_{green}/F_{red}) demonstrated a good linearity with the logarithmic concentration of Fe^{2+} in the range of 1-105 μM (Figure 2C) and detection limit (LOD) was achieved down to 210 nM (S/N=3). Compared with previously reported Fe^{2+} sensors,[14,17-19] our developed probe demonstrated wider detection linear range.

In order to confirm the high selectivity of this nanosensor toward Fe^{2+}, the absorption spectra of FeL were measured in the presence of various metal ions

including Fe^{2+}, Fe^{3+}, Zn^{2+}, Co^{2+}, Cu^{2+}, and so on. A distinct board absorption peak of FeL was observed around 575 nm only in the presence of Fe^{2+} while no obvious absorption peak was obtained for individual either FeL or Fe^{2+} (Figure S8A). Meanwhile, no absorption peaks were observed around 575 nm with addition of other metal ions. Furthermore, the absorption peak around 575 nm increased with the increasing concentration of Fe^{2+} (Figure S8B). Actually, this distinct absorption peak around 575 nm was considered as the metal-to-ligand charge-transfer (MLCT) band due to the formation of FeL-Fe^{2+} complex.[42] Because the compounds containing the -N=C-C=N- linkage, like 1,l0-phenanthroline and 2,2'-bipyridine, have been reported to be strong chelating agents for Fe^{2+},[43,44] FeL contains two -N=C-C=N- linkages may have stronger bonding capability toward Fe^{2+} against other metal ions.[17,45] These results demonstrated above have confirmed the high selectivity of FeL toward Fe^{2+} against other metal ions.

Besides, it has been reported that surface ligands can influence the fluorescence of AuNCs by charge transfer or electron donation.[41] The fluorescent emission of GSH-template AuNCs was attributed to the charge transfer from GSH to AuNC core.[46] However, the charge transfer process was disturbed after electron-withdrawing FeL was coupled onto the surface of AuNCs, resulting in the partial fluorescence decrease of AuNCs (Figure 1C). Then, after addition of Fe^{2+}, the charge transfer was enhanced from AuNCs to Fe^{2+} through the FeL-Fe^{2+} complex, leading to the fluorescence quench of AuNCs@FeL probe. Thus, owing to high specific of FeL

towards Fe^{2+}, the developed nanosensor showed remarkable selectivity towards Fe^{2+} against Fe^{3+} and other similar elements or environments.

Next, we investigated the response dynamic of nanosensor. As shown in Figure 2D, the responsive time of AuNC@FeL@Cy7 towards Fe^{2+} titration was less than ~1.23 s, which is very benefit for real-time imaging and biosensing of Fe^{2+} in live cells. For further determining Fe^{2+} in the complicated environments such as live cells, selectivity and competition test of the nanosensor for Fe^{2+} sensing were examined in detail. For selectivity test, different potential biological species such as metal ions including Fe^{3+}, K^{+}, Ca^{2+}, Na^{+}, Mg^{2+}, Cu^{2+}, Zn^{2+}, Ag^{+}, Co^{2+}, Ni^{2+}, Cd^{2+} and Mn^{2+}, amino acids, common reactive oxygen species (ROS) including $O_2^{\bullet-}$, NO, ROO•, and •OH, as well as Fe-containing proteins including hemoglobin, transferrin, and serum ferritin were investigated. As summarized, other metal ions, amino acids, ROS, and Fe-containing proteins showed negligible interferences (< 5.0%) (Figure S9). Moreover, pH in the range of 5.4-8.0 had no obvious influence on Fe^{2+} sensing (Figure S10). Moreover, competition test results demonstrated these potential interferences had negligible influence on determination of Fe^{2+} (< 4.0%) (Figure S9), providing a reliable platform for imaging and biosensing of Fe^{2+}. Considering high concentration of salts in live cells, we also investigated the fluorescence stability of nanosensor in the presence of different concentrations of NaCl. No obvious interferent of NaCl was observed on fluorescence of nanosensor even at a very high concentration of 1 M (Figure S11). This result suggests good stability of

AuNC@FeL@Cy7 against salt.

In addition, after exposing to a Xe lamp for 2.5 h, the fluorescent intensities of two emission signals demonstrated no obvious changes (< 3.9%), indicating long-term photostability of AuNC@FeL@Cy7 probe (Figure S12).

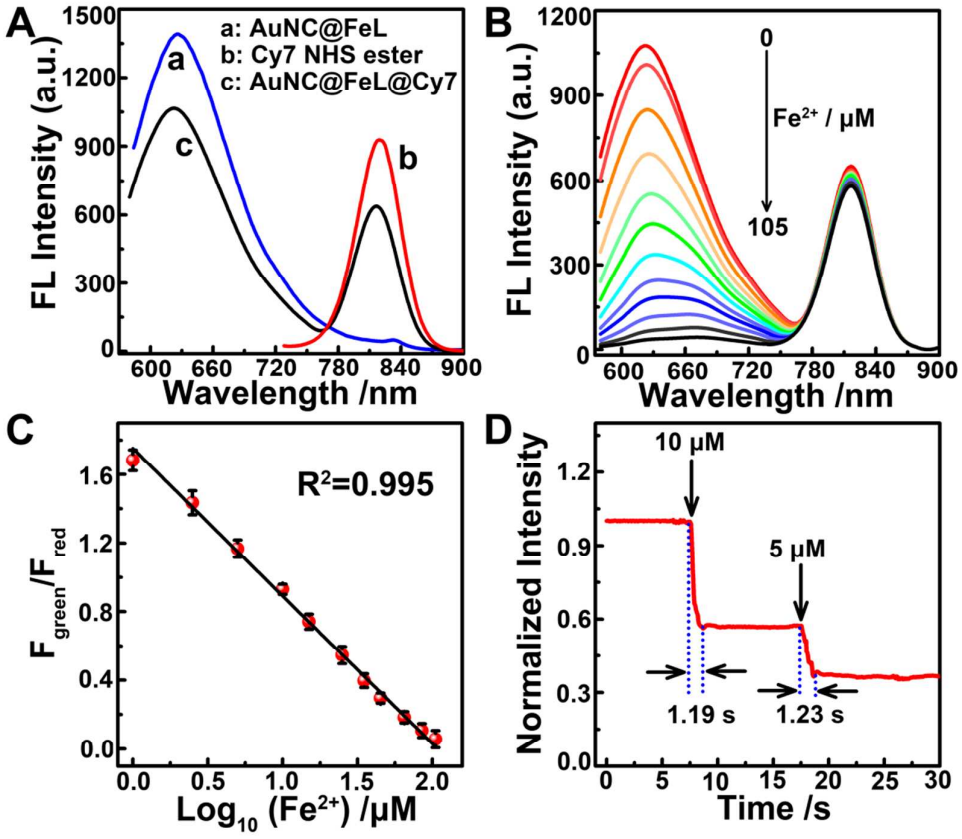

Figure 2. (A) Fluorescence emission spectra of (a) AuNC@FeL, (b) Cy7 NHS ester, and (c) AuNC@FeL@Cy7 probe. (B) Fluorescence spectra of AuNC@FeL@Cy7 upon addition of Fe^{2+} with different concentrations (0, 1, 2.5, 5, 10, 15, 25, 35, 45, 65, 85, and 105 μM) in cell lysis buffer. The excitation wavelength was 552 nm. (C) Linear calibration curve between F_{green}/F_{red} and various Fe^{2+} concentrations. F_{green} and F_{red} represent the fluorescence intensity collected from 580-760 nm and 765-900 nm, respectively. (D) Time-tacking of AuNC@FeL signal upon addition of 10 μM and 5 μM Fe^{2+} to AuNC@FeL@Cy7 solution. The fluorescence intensity was obtained at 619 nm while excited at 552 nm.

Multicolor imaging and biosensing of Fe^{2+}in Neurons. In order to realize further

biological applications, cytotoxicity and biocompatibility of the developed nanosensor towards HepG2 cells and neurons were examined. The cell viability maintained greater than 84% even at a higher dosage of 70 μM probes than that used for bioimaging in live cells (Figure S13), indicating low cytotoxicity of nanosensor to cells. Besides, the flow cytometry experiments demonstrated that no obvious different results were obtained in the present of various concentrations of AuNC@FeL@Cy7 probe, compared with control experiments (Figure S14-S15). These results demonstrate the low-cytotoxicity and good biocompatibility of the present fluorescent nanosensor. Taking remarkable advantages of the developed probe, bioimaging and biosensing of Fe^{2+} in neuron were firstly investigated. As shown in Figure 3A-D, after addition of exogenous Fe^{2+} with different concentrations, the fluorescence intensity of green channel (F_{green}: 580-760 nm) decreased distinctly while that of red channel (F_{red}: 765-900 nm) kept constant. The pseudo color of merged channel changed from orange-red to blue-green, the average fluorescent intensity ratio of green channel to red channel (F_{green}/F_{red}) decreased from 1.73±0.15 to 0.15±0.09 (Figure 3F), indicating the increasing concentration of Fe^{2+} in neuron. Besides, we found the concentration of Fe^{2+} in different regions of neuron was various. F_{green}/F_{red} value in soma of neuron was 1.44±0.14, which is higher than those in other regions, such as proximal axon (1.13±0.27), distal axon (0.52±0.21), and synaptic compartment (0.22±0.09) (Figure 3G). These results indicate the distribution of endogenous Fe^{2+} ion in neurons was unhomogeneous and the concentrations of Fe^{2+} in synaptic compartment and distal axon were higher than those in proximal axon and soma. For verifying that this fluorescence decrease was ascribed to Fe^{2+}-dependent events, 100 μM desferoxamine (DFO) - iron chelator was added in the presence of 75 μM Fe^{2+}. As expected in Figure 3E, DFO chelation prevented the fluorescence quench of green channel, certifying that the observed fluorescence decrease of green channel was indeed attributed to elevated levels of exogenous and exchangeable Fe^{2+}.

On the other hand, the similar results were also observed in HepG2 cells (Figure

S16). The observation suggests that the developed AuNC@FeL@Cy7 probe can be used for Fe^{2+} detection in different live cells. In addition, we carried out the co-localization experiments to estimate the targeting ability of nanosensor.[47] Hoechst 33342, MitoTracker Green, LysoTracker Green, and CellTracker Green CMFDA were used for targeting nucleus, mitochondria, lysosomes and cytoplasm, respectively. the fluorescence of AuNC@FeL@Cy7 probe poorly overlapped with those of Hoechst 33342, LysoTracker Green, and MitoTracker Green, and the Pearson's correlation coefficient (ρ) were calculated as 0.03, 0.1 and 0.35, respectively (Figure S17A-C). However, the fluorescence of AuNC@FeL@Cy7 probe merged well with that of CellTracker Green CMFDA (ρ=0.85) (Figure S17D). These results indicate that the developed AuNC@FeL@Cy7 probe was primary located in cytoplasm.

Next, in order to estimate the distribution of Fe^{2+} in HepG2 cells in the subcellular level, the nanosensors for targeting specific different organelles were further synthesized. Lysosomes play the important roles in cellular apoptosis, intracellular digestion, immunologic defense, and specialized secretory functions,[48,49] which are also the major targets of the iron-mediated peroxidative attack. Meanwhile, cellular pathogenesis is associated with iron-mediated hydrolases releasing from lysosomes.[50] On the other hand, mitochondria play crucial roles in energy metabolism, cellular differentiation and apoptosis, and are the main intracellular source of ROS.[51-53] Previous researches have showed that iron can induce oxidative damage in mitochondria by catalyzing the formation of •OH radicals.[54] Since mitochondria and lysosomes are important organelles in cells and have close relations with iron, (4-carboxybutyl) triphenylphosphonium bromide (TPP) and 4-(2-aminoethyl) morpholine (AMP) were coupled onto the surface of AuNC@FeL@Cy7 probe for targeting mitochondria and lysosomes according to the reported literature[47]. The AuNC@FeL@Cy7 probes conjugated with TPP and AMP were denoted as AuNC@FeL@Cy7@TPP and AuNC@FeL@Cy7@AMP, respectively. The modification processes were characterized by X-ray photoelectron spectroscopy

(XPS). XPS spectrum shows typical elements of C, N, O, Au in AuNC@FeL@Cy7@AMP probe (Figure S18A). A high resolution spectrum of O 1s exhibits three peaks at 530.6 eV (C=O), 531.4 eV (C-O-C) and 532.4 eV (C-O-H), respectively (Figure S18C). The peak of C-O-C belongs to the morpholine of AMP, indicating the successful attachment of AMP onto AuNC@FeL@Cy7 probe. Meanwhile, XPS survey spectrum of AuNC@FeL@Cy7@TPP probe shows obvious C, N, O, Au, P elements and individual XPS spectrum of P 2p region shows apparent peaks around 131.4 eV (Figure S18 B and D), strongly demonstrating TPP has been coupled on the AuNC@FeL@Cy7 probe. Then, the co-localization experiments were carried out for confirming the targeting ability of AuNC@FeL@Cy7@AMP and AuNC@FeL@Cy7@TPP probes toward lysosomes and mitochondria. The fluorescence of AuNC@FeL@Cy7@AMP merged well with the fluorescence of LysoTracker (ρ=0.91) while the fluorescence of AuNC@FeL@Cy7@TPP merged well with that of MitoTracker (ρ=0.94) (Figure S19), clearly demonstrating the developed AuNC@FeL@Cy7@AMP and AuNC@FeL@Cy7@TPP probes entered into cells and primary located in lysosomes and mitochondria, respectively.

Furthermore, AuNC@FeL@Cy7@AMP and AuNC@FeL@Cy7@TPP probes were used to investigate the Fe^{2+} distribution in different organelles, respectively. Different fluorescence ratios were obtained in various organelles (Figure S20A-C), and the fluorescence intensity ratio (F_{green}/F_{red}) in lysosomes (1.48±0.05) was similar with that in cytoplasm (1.5±0.04) (Figure S20D), indicating the concentration of Fe^{2+} in lysosomes was almost same as that in cytoplasm. Meanwhile, F_{green}/F_{red} value in mitochondria (1.34±0.05) was lower than those in lysosomes and cytoplasm, demonstrating that the concentration of Fe^{2+} in mitochondria was higher than those in cytoplasm and lysosome.

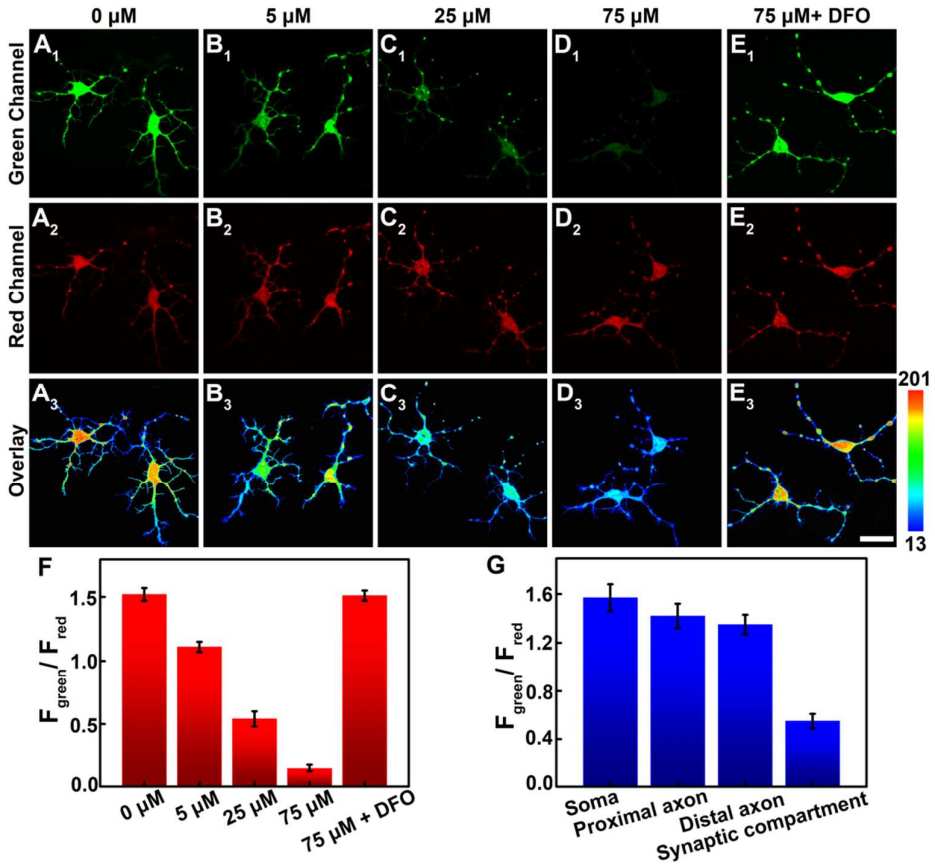

Figure 3. Confocal fluorescence microscopic images of neurons collected from different channels treated with AuNC@FeL@Cy7 probe (30 μM) in the presence of different concentrations of Fe^{2+}: (A_1-A_3) 0, (B_1-B_3) 5, (C_1-C_3) 25, and (D_1-D_3) 75 μM. (E_1-E_3) Confocal fluorescence microscopic images of neurons collected from different channels treated with AuNC@FeL@Cy7 probe (30 μM) in the presence of 75 μM Fe^{2+} followed by adding 100 μM DFO for 1 h. (F) Summarized data of average fluorescence intensity ratio (F_{green}/F_{red}) obtained from A-E. (G) F_{green}/F_{red} values of different neuronal regions (soma, proximal axon, distal axon, and synaptic compartment) in the absence of extracellular Fe^{2+} ion. The data was obtained based on the statistical analysis of more than 30 neurons. F_{green} and F_{red} represent the average fluorescence intensity collected from green channel (580-760 nm) and red channel (765-900 nm), respectively. The excitation wavelength was 552 nm. Scale = 25 μm.

Neuronal Fe^{2+} fluctuation under ischemic injury. Ischemic stroke as one of the most fatal diseases could result in disability or even death.[55,56] Recent research has

shown that cerebral ischemia may result in serious oxidative stress, which is close to neuronal death and brain injury.[57-59] Considering the important role of Fe^{2+} in oxidative stress,[6,7] investigation of relationship between Fe^{2+} and cerebral ischemia is helpful for understanding the molecular mechanism of ischemia-induced brain injury.

Next, AuNC@FeL@Cy7 probe was applied for neuronal Fe^{2+} sensing and imaging under oxygen and glucose deprivation (OGD) treatment, an ischemic injury cell model, which has been well-established to investigate the mechanism of ischemia-induced cell death.[60,61] Confocal images were obtained after OGD treatment for different times. As shown in Figure 4A-G, the fluorescent intensity of green channel weakened distinctly with the extension of OGD treating time. Meanwhile, no noticeable change was observed from the red channels. From the merged image, it was found the pseudo color of neuron changed from orange-red to blue-green, and F_{green}/F_{red} value decreased from 1.57±0.06 to 0.69±0.06 (Figure 4I), suggesting an expansion of labile Fe^{2+} pools in the treatment of OGD. However, this intracellular Fe^{2+} increase was cut down obviously after reinstatement of supplying oxygen and glucose (Figure 4H), proving that expansion of labile Fe^{2+} pools in neuron as a result of OGD treatment. It should be noted that neurons were cultured in PBS without iron ions during OGD treatment, indicating that the increased neuronal Fe^{2+} was possibly due to a mobilization of iron stores into a labile form and/or transition between Fe^{2+} and Fe^{3+}. These results strongly imply that Fe^{2+} takes crucial character in ischemia-induced brain injury.

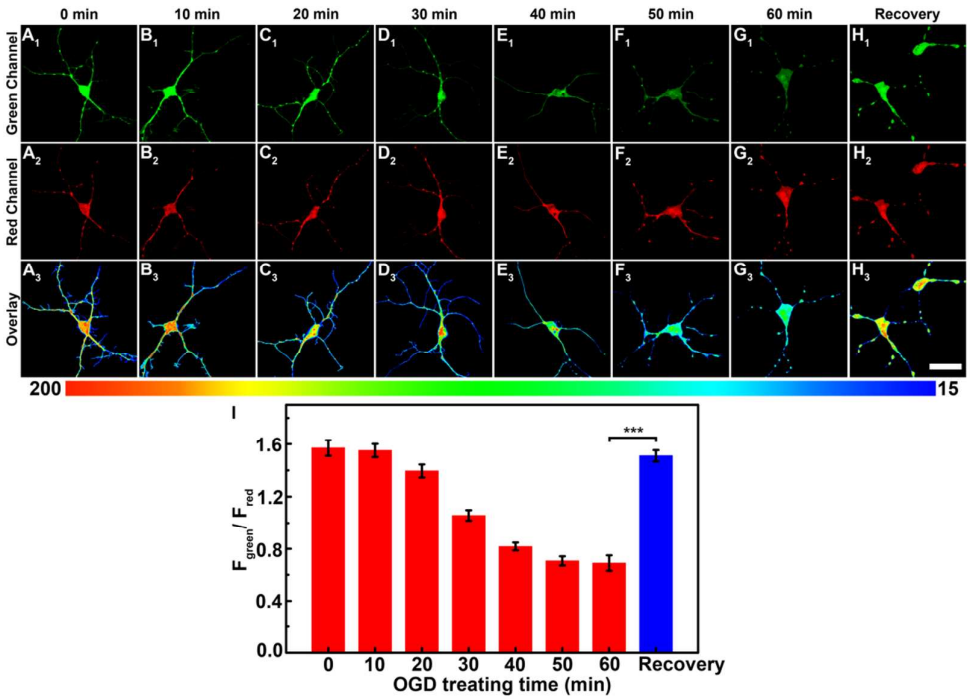

Figure 4. Confocal fluorescence microscopic images of neurons co-incubated with AuNC@FeL@Cy7 probe (30 μM) for 1 h, followed by OGD treatment for (A_1-A_3) 0, (B_1-B_3) 10, (C_1-C_3) 20, (D_1-D_3) 30, (E_1-E_3) 40, (F_1-F_3) 50, and (G_1-G_3) 60 min. (H_1-H_3) Confocal fluorescence microscopic images of neurons first treated with OGD for 60 min, then cultured with oxygen and glucose for 60 min, followed by incubating with AuNC@FeL@Cy7 probe (30 μM) for 1 h. (I) Summarized data of average fluorescence intensity ratio (F_{green}/F_{red}) obtained from A-H. The data were obtained based on the statistical analysis of more than 30 neurons (n = 3-4, $^{*}P<0.05$, $^{**}P<0.01$, $^{***}P<0.001$, NS means no statistical significance, by unpaired t-test). F_{green} and F_{red} represent the average fluorescence intensity collected from green channel (580-760 nm) and red channel (765-900 nm), respectively. The excitation wavelength was 552 nm. Scale = 25 μm.

Hypoxia-induced fluctuation of Fe^{2+} in HepG2 cells. As well-known that oxygen is vital for cancer growth and recent research has demonstrated that deoxygenation agent for cancer starvation therapy is a potentially useful strategy in fighting cancer.[37] Furthermore, the stability of intracellular Fe^{2+} is highly dependent on the oxidative stress level, which would be activated by hypoxic conditions.[36,62] Thus, we further

investigated the variation of Fe^{2+} in HepG2 cells after hypoxia treatment with Mg_2Si nanoparticles (MSPs) under tumor microenvironment as a model. As shown in Figure 5A, the prepared MSPs were monodispersed with irregular morphology. Besides, MSPs show typical crystal lattice of with noticeable serrated edges (Figure 5B), suggesting the successful preparation of MSPs.[37]

Then, intracellular O_2 level was first characterized by indicator of [Ru(4,7-diphenyl-1,10-phenanthroline)$_3$]Cl_2. As shown in Figure 5C, after treated with 3 mM MSPs for 1 h at pH 7.4, fluorescence of O_2 indicator showed no obvious change. But the red fluorescence of indicator increased distinctly after treated with 3 mM MSPs for 1 h at pH 6.5, indicating the effective O_2 scavenging in cell in an acidic environment and the significant deoxygenation effect was generated because the silane released from Mg_2Si, which efficiently reacts with oxygen to form silicon oxide (SiO_2) aggregates.[37] Then, we investigated the changes of Fe^{2+} concentration in HepG2 cells under hypoxia stimulated by MSPs. As shown in Figure 5D, both fluorescence intensity of green channel and red channel demonstrated no evident changes after treated with 3 mM MSPs for 1 h, revealing the negligible changes of intracellular Fe^{2+}. However, after treated with 3 mM MSPs for 1 h at pH 6.5, the fluorescence intensity of green channel decreased apparently while red channel kept stable (Figure 5E), clearly showing that the intracellular Fe^{2+}

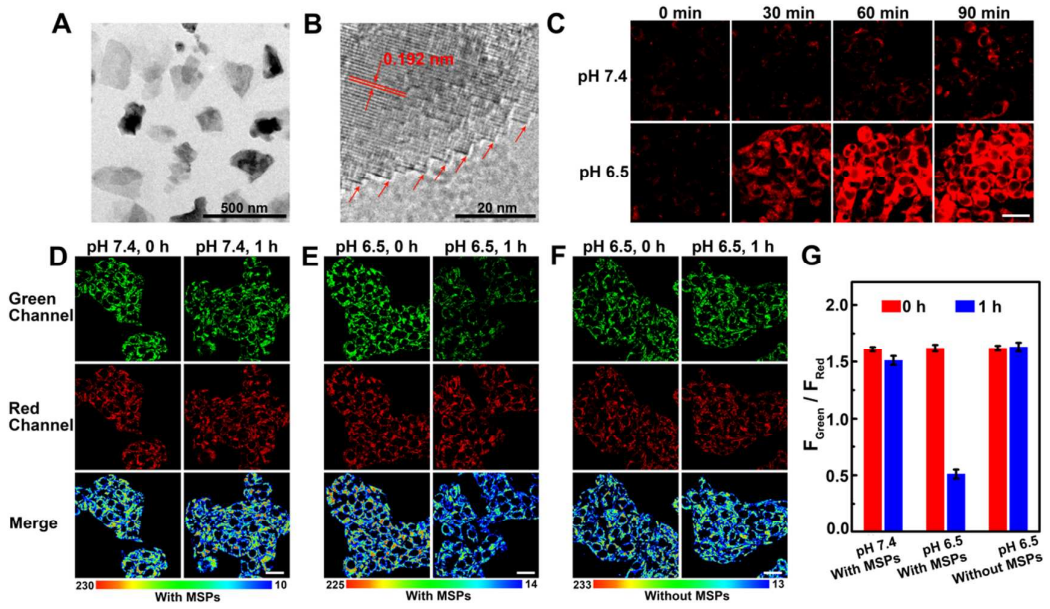

Figure 5. (A) TEM image of highly dispersed MSPs. (B) Close-up high-resolution TEM image of MSPs with serrated edge (highlighted by red arrows). (C) Confocal images of intracellular O_2 level indicator $[Ru(dpp)_3]Cl_2$-stained HepG2 cells after treating at pH 7.4 or 6.5 co-incubated with 3 mM MSPs for various times (0, 30, 60 , 90 min). The fluorescence signal was obtained between 500-700 nm at excitation wavelength of 488 nm. (D) Confocal images of MSPs-treated HepG2 cells at pH 7.4 in the present of AuNC@FeL@Cy7 probe. (E) Confocal images of MSPs-treated HepG2 cells at pH 6.5 in the present of AuNC@FeL@Cy7 probe. (F) Confocal images of HepG2 cells at pH 6.5 in the present of AuNC@FeL@Cy7 probe. (G) Summarized data of F_{green}/F_{red} values in D, E, and F. F_{green} and F_{red} represent the average fluorescence intensity collected from green channel (580-760 nm) and red channel (765-900 nm), respectively. The excitation wavelength was 552 nm. Scale bars=25 μm.

concentration increased under hypoxia stimulation. It should be noted that negligible changes were observed at both channels of green and red at pH 6.5 without MSPs (Figure 5F). As summarized in Figure 5G, F_{green}/F_{red} value decreased to 1.11±0.02 after deoxidizing treatment at pH 6.5 while negligible change was observed either at pH 7.4 with deoxidizing treatment or at pH 6.5 without deoxidizing treatment. It has

been reported that oxidative stress can cause fluctuation of redox balance of Fe^{2+} and the stability of Fe^{2+} in aqueous buffer is highly dependent on concentration of dissolved oxygen,[36,62,63] thus, hypoxia treatment may result in oxidative stress by inducing Fe^{2+} increase in HepG2 cells.

CONCLUSIONS

In summary, a AuNCs-based ratiometric fluorescence nanosensor has been developed for intracellular sensing and imaging of Fe^{2+}, in which FeL has been designed as a selective recognition molecule and Cy7 as an inn-reference element. This ratiometric fluorescent nanosensor has realized sensitive detection of Fe^{2+} with high accuracy, good stability and fast response dynamics, as well as remarkable selectivity against metal ions, amnion acids, common ROS and Fe-containing proteins. Furthermore, the developed nanosensor has demonstrated low cytotoxicity and good compatibility, and eventually applied in multicolor imaging and biosensing of Fe^{2+} in neurons and HepG2 cells. Using this useful tool, it has been found the distribution of neuronal Fe^{2+} was unhomogeneous and mitochondrial Fe^{2+} was higher than those in cytoplasm and lysosome in HepG2 cells. Besides, we found Fe^{2+} takes crucial character in ischemia-induced brain injury. The developed nanosensor has also provided an established method to investigate the function of Fe^{2+} in oxidative stress and further to understand the molecular mechanism related to biological and pathological processes of oxidative stress-induced diseases. Moreover, we have also

found that the concentration of Fe^{2+} increases upon hypoxia under acidic environment, which may provide a new sight to understand the function of Fe^{2+} in cancer starvation therapy.

ASSOCIATED CONTENT

The Supporting Information is available free of charge on the ACS Publications website. Synthesis and characterization of FeL; UV-vis absorption spectrum of AuNCs and FT-IR characterization of AuNC@FeL@Cy7 probe; Selectivity of AuNC@FeL@Cy7 probe; Stability investigation of AuNC@FeL@Cy7 probe; Cytotoxicity and biocompatibility study of AuNC@FeL@Cy7 probe; Confocal fluorescence imaging of HepG2 cells.

AUTHOR INFORMATION

Corresponding Author

*Phone: + 86 21 54341041; fax: +86 21 54341041; E-mail: ytian@chem.ecnu.edu.cn

Notes

[+]These authors contributed equally to this work. The authors declare no competing financial interest.

ACKNOWLEDGMENT

This work was financially supported by National Nature Science Fund for Distinguished Young Scholars (21325521) and NSFC (21635003). The Program of

Shanghai Subject Chief Scientist (15XD1501600) and support from China Postdoctoral Science Foundation (2014M561436 and 2016T9349) are gratefully acknowledged.

REFERENCES

(1) Wilson, M. T.; Reeder, B. J. *Exp. Physiol.* **2008**, *93*, 128-132.

(2) Aisen, P.; Wessling-Resnick, M.; Leibold, E. A. *Curr. Opin. Chem. Biol.* **1999**, *3*, 200-206.

(3) Costas, M.; Mehn, M. P.; Jensen, M. P.; Que, L. *Chem. Rev.* **2004**, *104*, 939-986.

(4) Rouault, T. A.; Wing-Hang, T. *Nat. Rev. Mol. Cell Biol.* **2005**, *6*, 345.

(5) Williams, R.; Da Silva, J. F. *Coord. Chem. Rev.* **2000**, *200*, 247-348.

(6) Dixon, S. J.; Stockwell, B. R. *Nat. Chem. Biol.* **2013**, *10*, 9-17.

(7) Enami, S.; Sakamoto, Y.; Colussi, A. J. *Proc. Natl. Acad. Sci. U.S.A.* **2014**, *111*, 623-628.

(8) Lee, T. W.; Kolber, M. R.; Fedorak, R. N.; van Zanten, S. V. *Journal of Crohn's and Colitis* **2012**, *6*, 267-275.

(9) Fishbane, S.; Singh, A. K. *Kidney Int.* **2009**, *75*, 752-754.

(10) Kowdley, K. V. *Gastroenterology* **2004**, *127*, 79-86.

(11) Oshiro, S.; Morioka, M. S.; Kikuchi, M. *Adv. Pharmacol. Sci.* **2011**, *2011*, 378278-378278.

(12) Crichton, R. R.; Dexter, D. T.; Ward, R. J. *J. Neural Transm.* **2011**, *118*, 301-314.

(13) Shamspur, T.; Sheikhshoaie, I.; Mashhadizadeh, M. H. *J. Anal. At. Spectrom.* **2005**, *20*, 476-478.

(14) Den Berg, C. M. G. V. *Anal. Chem.* **2006**, *78*, 156-163.

(15) Arnold, G. L.; Weyer, S.; Anbar, A. D. *Anal. Chem.* **2004**, *76*, 322-327.

(16) Stookey, L. L. *Anal. Chem.* **1970**, *42*, 779-781.

(17) Li, P.; Fang, L.; Zhou, H.; Zhang, W.; Wang, X.; Li, N.; Zhong, H.; Tang, B. *Chem. Eur. J.* **2011**, *17*, 10520-10523.

(18) Aron, A. T.; Loehr, M. O.; Bogena, J.; Chang, C. J. *J. Am. Chem. Soc* **2016**, *138*, 14338-14346.

(19) Au-Yeung, H.; Chan, J.; Chantarojsiri, T.; Chang, C. *J. Am. Chem. Soc.* **2013**, *135*, 15165-15173.

(20) Spangler, B.; Morgan, C. W.; Fontaine, S. D.; Vander Wal, M. N.; Chang, C. J.; Wells, J. A.; Renslo, A. R. *Nat. Chem. Biol.* **2016**, *12*, 680-685.

(21) Kim, S.; Tachikawa, T.; Fujitsuka, M.; Majima, T. *J. Am. Chem. Soc.* **2014**, *136*, 11707-11715.

(22) Naito, K.; Tachikawa, T.; Fujitsuka, M.; Majima, T. *J. Phys. Chem. C* **2008**, *112*, 1048-1059.
(23) Setsukinai, K.-i.; Urano, Y.; Kakinuma, K.; Majima, H. J.; Nagano, T. *J. Biol. Chem.* **2003**, *278*, 3170-3175.
(24) Kong, B.; Zhu, A.; Ding, C.; Zhao, X.; Li, B.; Tian, Y. *Adv. Mater.* **2012**, *24*, 5844-5848.
(25) Zhu, A.; Qu, Q.; Shao, X.; Kong, B.; Tian, Y. *Angew. Chem. Int. Ed.* **2012**, *51*, 7185-7189.
(26) Fu, Y.; Ding, C.; Zhu, A.; Deng, Z.; Tian, Y.; Jin, M. *Anal. Chem.* **2013**, *85*, 11936-11943.
(27) Gao, X.; Ding, C.; Zhu, A.; Tian, Y. *Anal. Chem.* **2014**, *86*, 7071-7078.
(28) Han, Y.; Ding, C.; Zhou, J.; Tian, Y. *Anal. Chem.* **2015**, *87*, 5333-5339.
(29) Huang, H.; Dong, F.; Tian, Y. *Anal. Chem.* **2016**, *88*, 12294-12302.
(30) Li, W.; Fang, B.; Jin, M.; Tian, Y. *Anal. Chem.* **2017**, *89,* 2553-2560.
(31) Zhuang, M.; Ding, C.; Zhu, A.; Tian, Y. *Anal. Chem.* **2014**, *86*, 1829-1836.
(32) Shi, W.; Li, X.; Ma, H. *Angew. Chem. Int. Ed.* **2012**, *51*, 6432-6435.
(33) Liu, J.-M.; Chen, J.-T.; Yan, X.-P. *Anal. Chem.* **2013**, *85*, 3238-3245.
(34) Wan, Q.; Chen, S.; Shi, W.; Li, L.; Ma, H. *Angew. Chem. Int. Ed.* **2014**, *53*, 10916.
(35) Wang, X.; Sun, J.; Zhang, W.; Ma, X.; Lv, J.; Tang, B. *Chem. Sci.* **2013**, *4*, 2551-2556.
(36) Hirayama, T.; Tsuboi, H.; Niwa, M.; Miki, A.; Kadota, S.; Ikeshita, Y.; Okuda, K.; Nagasawa, H. *Chem. Sci.* **2017**, *8,* 4858-4866.
(37) Zhang, C.; Ni, D.; Liu, Y.; Yao, H.; Bu, W.; Shi, J. *Nat. Nanotechnol.* **2017**, *12,* 378-386.
(38) Gao, J.; Duan, B.; Wang, D.-G.; Deng, X.-H.; Zhang, G.-Y.; Xu, L.; Xu, T.-L. *Neuron* **2005**, *48*, 635-646.
(39) Luo, Z.; Yuan, X.; Yu, Y.; Zhang, Q.; Leong, D. T.; Lee, J. Y.; Xie, J. *J. Am. Chem. Soc.* **2012**, *134*, 16662-16670.
(40) Wen, Q.; Gu, Y.; Tang, L.-J.; Yu, R.-Q.; Jiang, J.-H. *Anal. chem.* **2013**, *85*, 11681-11685.
(41) Wu, Z.; Jin, R. *Nano Lett.* **2010**, *10*, 2568-2573.
(42) Maiti, S.; Aydin, Z.; Zhang, Y.; Guo, M. *Dalton Trans.* **2015**, *44*, 8942-8949.
(43) Lee, T.; Kolthoff, I.; Leussing, D. *J. Am. Chem. Soc.* **1948**, *70*, 2348-2352.
(44) Baxendale, J.; George, P. *Trans. Faraday Soc.* **1950**, *46*, 736-744.
(45) Martin, R. B.; Lissfelt, J. A. *J. Am. Chem. Soc.* **1956**, *78*, 938-940.
(46) Stamplecoskie, K. G.; Chen, Y.-S.; Kamat, P. V. *J. Phys. Chem. C* 2014, *118*, 1370-1376.
(47) Pan, W.; Wang, H.; Yang, L.; Yu, Z.; Li, N.; Tang, B. *Anal. Chem.* **2016**, *88*, 6743-6748.
(48) Saftig, P.; Klumperman, J. *Nat. Rev. Mol. Cell Biol.* **2009**, *10*, 623-635.
(49) Watts, C. *Biochim. Biophys. Acta* **2012**, *1824*, 14-21.
(50) Mak, I.; Weglicki, W. *J. Clin. Invest.* **1985**, *75*, 58-63.
(51) Kowaltowski, A. J.; Castilho, R. F.; Vercesi, A. E. *FEBS Lett.* **2001**, *495*, 12-15.
(52) Levine, B.; Kroemer, G. *Cell* **2008**, *132*, 27-42.
(53) McBride, H. M.; Neuspiel, M.; Wasiak, S. *Current biology* **2006**, *16*, R551-R560.
(54) Hermes-Lima, M.; Castilho, R. F.; Meinicke, A. R.; Vercesi, A. E. *Mol. Cell. Biochem.* **1995**, *145*, 53-60.

(55) Rossi, D. J.; Brady, J. D.; Mohr, C. *Nat. Neurosci.* **2007**, *10*, 1377-1386.

(56) Almajed, A. A.; Alomar, F. A.; Nagi, M. N. *Eur. J. Pharmacol.* **2006**, *543*, 40-47.

(57) Kamada, H.; Yu, F.; Nito, C.; Chan, P. H. *Stroke* **2007**, *38*, 1044-1049.

(58) Wang, Q.; Tompkins, K. D.; Simonyi, A.; Korthuis, R. J.; Sun, A. Y.; Sun, G. Y. *Brain Res.* **2006**, *1090*, 182-189.

(59) Love, S. *Brain Pathology* **1999**, *9*, 119-131.

(60) Tabakman, R.; Lazarovici, P.; Kohen, R. *J. Neurosci. Res.* **2002**, *68*, 463-469.

(61) Plesnila, N.; Zinkel, S.; Le, D. A.; Amin-Hanjani, S.; Wu, Y.; Qiu, J.; Chiarugi, A.; Thomas, S. S.; Kohane, D. S.; Korsmeyer, S. J. *Proc. Natl. Acad. Sci. U.S.A.* **2001**, *98*, 15318-15323.

(62) Sung, W.; Morgan, J. J. *Environ. Sci. Technol.* **1980**, *14*, 561-568.

(63) Hider, R. C.; Kong, X. L. *BioMetals* **2011**, *24*, 1179-1187.

For TOC only